Supplement of Atmos. Chem. Phys., 26, 13303–13318, 2026
https://doi.org/10.5194/acp-26-13303-2026-supplement

Atmospheric Chemistry and Physics
Open Access
EGU

Supplement of

Apportioning light absorption of ambient aerosols to black carbon, brown carbon, and lensing effect using a PAX-ISS hybrid method: insights into absorption enhancement

Yi Shen et al.

Correspondence to: Guorui Zhi (zhigr@craes.org.cn) and Yuzhe Zhang (yzzhang943@foxmail.com)

Section S1 Quality assurance measures for the sampling filters

A high-volume sampler was used to collect $PM_{2.5}$ samples on 8″ × 10″ quartz filters. Prior to sampling, the quartz filters were pre-baked at 550°C for 6 hours to remove adsorbed organics. Field blanks were also analysed to account for background contamination, and their concentrations were subtracted from the sample results. Filters deposited with $PM_{2.5}$ were stored at -20°C until thermal/optical analysis or integrating sphere analysis of carbonaceous aerosols was conducted.

The mass concentration of $PM_{2.5}$ (μg/m^3) collected on each filter was calculated according to the following formula:

$$PM_{2.5} = \frac{M_{collected} - M_{blank}}{V_{air}}, \quad \text{(S1)}$$

where $M_{\text{collected}}$ and M_{blank} represent the sample- and blank-filter masses (μg), respectively, and V_{air} represents the air volume (m^3) that accommodated the collected particulate matter. An analytical balance with a precision of 0.1 mg was used to obtain highly accurate mass measurements in the laboratory environment.

$PM_{2.5}$ samples were collected daily. Each filter was used for one day, from 9:00 a.m. on the first day to 8:30 a.m. the following day. The eligible days of $PM_{2.5}$ sampling are detailed in Table S1.

Table S1. Eligible days of $PM_{2.5}$ sampling.

Winter	Spring	Summer	Autumn
2/9/2023	4/7/2023	7/7/2023	10/12/2023
2/10/2023	4/8/2023	7/8/2023	10/13/2023
2/12/2023	4/9/2023	7/9/2023	10/14/2023
2/13/2023	4/10/2023	7/10/2023	10/15/2023
2/14/2023	4/11/2023	7/11/2023	10/16/2023
2/15/2023	4/12/2023	7/12/2023	10/17/2023
2/16/2023	4/13/2023	7/13/2023	10/18/2023
2/17/2023	4/17/2023	7/14/2023	10/19/2023
2/18/2023	4/18/2023	7/15/2023	10/20/2023
2/19/2023	4/19/2023	7/16/2023	10/21/2023
2/20/2023	4/20/2023	7/17/2023	10/22/2023
2/21/2023	4/24/2023	7/18/2023	10/23/2023
2/22/2023	4/25/2023	7/19/2023	10/24/2023
2/23/2023	4/26/2023	7/20/2023	10/25/2023
2/24/2023	4/27/2023	7/21/2023	10/26/2023
	4/28/2023	7/22/2023	10/27/2023
	4/29/2023	7/23/2023	10/28/2023
	4/30/2023	7/24/2023	10/29/2023
	5/1/2023	7/25/2023	10/30/2023
	5/2/2023	7/26/2023	10/31/2023
	5/3/2023	7/27/2023	11/1/2023
	5/5/2023	7/28/2023	11/2/2023
	5/6/2023	7/29/2023	11/3/2023
	5/7/2023	7/30/2023	11/4/2023
	5/8/2023	7/31/2023	11/5/2023
	5/9/2023	8/1/2023	
		8/2/2023	
		8/3/2023	
		8/4/2023	
		8/5/2023	
		8/6/2023	

Section S2 Measurement of conversion factor

The sample holder inside the integrating sphere chamber (ISS) absorbs light from multiple directions rather than a single direction. As a result, the absorbance measured by the IS system (ABS_{ISS}) differs from that obtained using conventional methods (ABS), in which the incident light comes from one direction only. Photoacoustic spectroscopy (PAX) is also considered a conventional method. To convert ABS_{ISS} to ABS, a conversion factor (CF) was determined by comparing the absorbances of Humic Acid Sodium Salt (HASS) obtained from the ISS system (ABS_{ISS}) and from conventional methods (ABS) (e.g., using a cuvette outside the integrating sphere).

$$CF = \frac{ABS_{ISS}}{B_{abs}} \quad (S2)$$

Specifically, a 40 μg/ml aqueous solution of HASS was first prepared in a volumetric flask. Then, 3 ml of the solution was drawn using a pipette and transferred into a 1 cm × 1 cm × 4 cm cuvette. The cuvette was placed into the sample holder inside ISS, and the ABS_{ISS} of the HASS solution was measured. Another 3 ml aliquot of the same HASS solution was transferred into an identical cuvette and placed in the sample holder outside the ISS. The conventional absorbance (ABS) was then measured following principles and procedures similar to those of standard spectrophotometers. Both ABS_{ISS} and ABS were measured relative to pure water. The CF value determined in this study was 2.0.

Section S3 Calculation and correction of absorption values in thermal/optical analysis

The 7-wavelength transmission laser signals from the DRI Model 2015 were used to calculate the light attenuation (*ATN*):

$$ATN(\lambda) = -ln\frac{I_i(\lambda)}{I_f(\lambda)} \ , \quad \text{(S3)}$$

where I_i and I_f are the light intensities transmitted through the filter before (i = initial) and after (f = final) thermal carbon analysis. The absorption coefficients were calculated based on the corrected $ATN(\lambda)$ values, taking into account the filter's multiple scattering and particulate loading (Chen et al., 2015; Chow et al., 2018; Peng et al., 2020). The loading effect refers to the decrease in light attenuation due to "overloading", also known as the shadowing effect (Cheng et al., 2011; Chow et al., 2018; Li et al., 2020; Ram and Sarin, 2009; Virkkula et al., 2007). The multiple-scattering effect arises from the filter matrix itself, which makes the total light attenuation through the filter noticeably higher than the actual absorption coefficient (B_{abs}) (Arnott et al., 2005b; Weingartner et al., 2003). We used the same correction method as in Chow et al. (2021), where samples were classified into 14 ranges with increments of 1 to 5 μg/cm^2 of EC filter loadings. $ATN(\lambda)$ values diminish with increased EC loadings. *ATN* at each wavelength was then adjusted upward to compensate for this decrease. The corrected $ATN(\lambda)$ is linearly related to EC loading and, generally, to the light absorption coefficient (B_{abs}). Such adjustment factors for EC loadings at different wavelengths were originally given in Chow et al (2021) and are presented here in Table S2.

Since aerosol absorption decreases exponentially with increasing wavelength, the effective absorption Ångström exponent (AAE_e) can be estimated by fitting all seven wavelengths with a derived coefficient (C):

$$ATN(\lambda) = C \times \lambda^{-AAE_e} \quad \text{(S4)}$$

Table S2 Attenuation adjustment factors for different EC loadings and wavelengths (Chow et al., 2021).

EC range (μg/cm^2)	ATN_{405}	ATN_{445}	ATN_{532}	ATN_{635}	ATN_{780}	ATN_{808}	ATN_{980}
0-3	1	1	1	1	1	1	1
3-4	1.21	1.19	1.17	1.12	1.13	1.12	1.14
4-5	1.32	1.28	1.25	1.18	1.18	1.18	1.2
5-6	1.42	1.36	1.31	1.23	1.22	1.22	1.24
6-7	1.5	1.43	1.36	1.26	1.25	1.24	1.26
7-8	1.58	1.5	1.43	1.3	1.29	1.29	1.3
8-9	1.64	1.55	1.46	1.33	1.31	1.31	1.33
9-10	1.72	1.62	1.51	1.36	1.33	1.34	1.34
10-11	1.79	1.68	1.57	1.41	1.38	1.38	1.39
11-13	1.88	1.75	1.62	1.45	1.41	1.41	1.42
13-16	2.07	1.91	1.75	1.53	1.49	1.48	1.48
16-20	2.36	2.17	1.99	1.71	1.65	1.66	1.66
20-25	2.71	2.53	2.3	1.97	1.91	1.91	1.93
>25	3.6	3.31	3.07	2.62	2.53	2.53	2.51

Section S4 Dual-Wavelength Iterative Calculation for Quantifying BC and BrC Absorbance

Calibration curves were established for Carbon Black (CarB) masses ranging from 3 μg to 21 μg and Humic Acid Sodium Salt (HASS) masses ranging from 5 μg to 72 μg. These curves relate mass to absorbance measured by the instrument at both 650 nm and 420 nm (Figure S2). CarB and HASS served as calibration standards for Black Carbon (BC) and Brown Carbon (BrC), respectively. The use of two wavelengths is essential due to the distinct spectral dependence of BC and BrC absorption, which enables their mathematical separation through the iterative calculation. Atmospheric BrC is chemically and optically heterogeneous; therefore, HASS is used here as a calibration surrogate rather than as an assumption that ambient BrC has the same chemical composition or absolute optical properties as HASS. HASS has been widely used in ISS-based BC/BrC separation (e.g., Wonaschütz et al., 2009; Sun et al., 2021; Wang et al., 2021). Other BrC surrogates, such as Suwannee River Fulvic Acid (SRFA; Kwon et al., 2018), could in principle be used in the DWIC procedure, but their wavelength-specific calibration relationships at 420 and 650 nm would need to be established under the same ISS conditions and be sufficiently distinct from those of CarB for stable dual-wavelength separation. A higher AAE than CarB alone is therefore not sufficient to guarantee quantitatively identical DWIC results. Nitroaromatic compounds can also be important atmospheric BrC chromophores (Lin et al., 2016), further illustrating that the choice of BrC surrogate may influence the quantitative BC/BrC partitioning. Accordingly, the surrogate choice is treated as a source of methodological uncertainty.

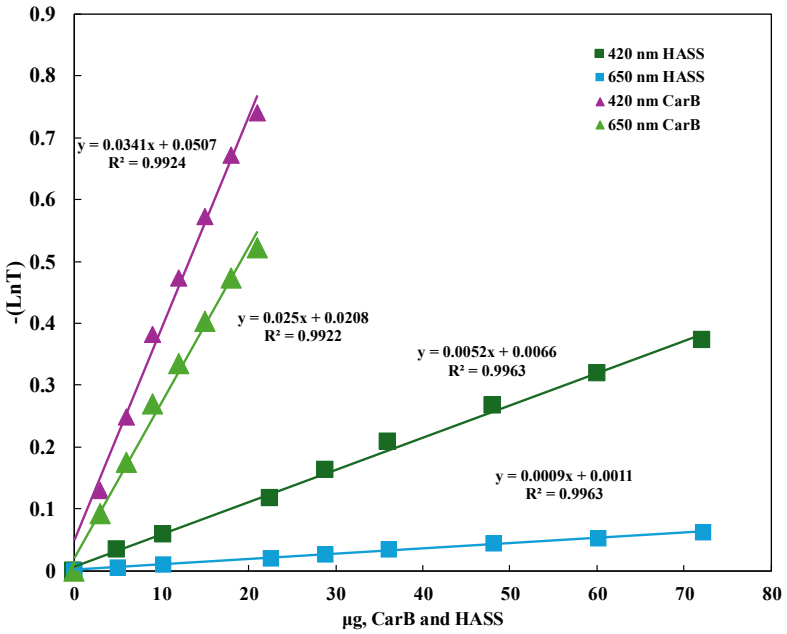

Figure S1 Calibration curves for CarB and HASS at 420 nm and 650nm. T represents the light transmitted through the calibration solution; (-lnT) is absorbance.

The iterative procedure is as follows:

1. Initial BC mass calculation (650 nm): Initiate an iteration cycle by calculating the BC mass. At 650 nm, the total absorbance is initially assumed to originate solely from BC. This mass (m_{BC}) is calculated using the CarB calibration equation at 650 nm (y = 0.025x + 0.0208).
2. BC absorbance at 420 nm: Substitute the obtained m_{BC} into the CarB calibration equation at 420 nm (y = 0.0341x + 0.0507) to calculate the absorbance attributable to BC at 420 nm ($A_{BC,420}$).
3. BrC absorbance at 420 nm: Subtract $A_{BC,420}$ from the measured total absorbance at 420 nm ($A_{total,420}$). The residual absorbance is attributed to BrC ($A_{BrC,420}$).
4. BrC Mass calculation: Substitute $A_{BrC,420}$ into the HASS calibration equation at 420 nm (y = 0.0052x + 0.0066) to calculate the BrC mass (m_{BrC}).
5. BrC absorbance at 650 nm: Substitute m_{BrC} into the HASS calibration equation at 650 nm (y = 0.0009x + 0.0011) to calculate the absorbance attributable to BrC at 650 nm ($A_{BrC,650}$).
6. Refined BC absorbance at 650 nm: Subtract $A_{BrC,650}$ from the measured total

absorbance at 650 nm ($A_{total,650}$). The residual absorbance at 650 nm is now attributed to BC ($A_{BC,650}$).

7. Convergence check & next cycle: Use the refined $A_{BC,650}$ to start a new iteration cycle by returning to step (1). Iteration continues until the calculated absorbances for both BC and BrC converge (i.e., when the difference between two consecutive iterative cycles is negligible). The absorbances from the final convergent cycle are accepted as the true absorbances for BC and BrC in the sample.

Section S5 ISS-PAX System Quality Control

Multiple measures during the experiment and data processing are conducted to minimize measurement uncertainties.

For the PAX measurements, although this instrument is commonly used as a key tool for in situ absorption measurements, it is not error-free. Therefore, we provide details regarding PAX measurement accuracy, calibration, and humidity control.

During the observation period, to improve the dryness of the gas entering the PAX instrument chamber, a preconditioning system consisting of a desiccant cylinder was set up (see Figure S2) to pre-dry the sampled airflow. The cylinder was mainly filled with molecular sieve material to adsorb moisture from the air. At the end of the drying cylinder near the PAX inlet, a section of color-indicating silica gel was installed as an indicator to visually show the drying efficiency: when the silica gel turns pink, it indicates that the molecular sieve is approaching water saturation, signaling a decline in the performance of the drying system and the need to replace the desiccant material in time.

To ensure the measurement accuracy and long-term stability of the PAX instrument, the device is sent back to the manufacturer, Nanjing Handa Environmental Technology Co., Ltd., every six months for routine calibration, maintenance, or replacement of critical components such as the vacuum pump, filter, and laser. The manufacturer provides formal maintenance records for each service, ensuring that the instrument remains in optimal working condition.

In addition, after each sampling period, routine cleaning of the instrument chamber is required to remove any residual particles that may have deposited inside, preventing contaminants from interfering with subsequent measurements. It is worth noting that Radney and Zangmeister (2017) identified fluctuations in the laser signal intensity within the PAX system as an important source of measurement uncertainty. To minimize such errors, prior to each sampling, the positions of two mirrors in the optical path are adjusted to maximize the laser beam signal intensity while keeping the

absorption and scattering coefficients at relatively low levels. This procedure helps to enhance the optical response sensitivity of the system under low black carbon concentrations, thereby improving measurement accuracy and reproducibility.

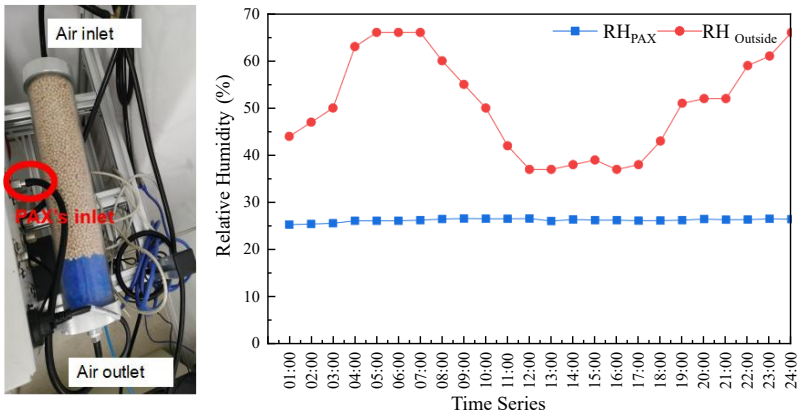

Figure S2 PAX drying system and drying performance.

For the thermal/optical analysis, we followed Chow et al. (2021) and applied wavelength- and EC-loading-dependent corrections to the multi-wavelength ATN data to reduce the effects of filter loading and multiple scattering on the spectral slope. Before daily instrumental analysis, three procedures, namely bake, blank, and calibration, were sequentially performed to remove impurities inside the instrument by combustion, determine the instrumental background value, which was subsequently subtracted during data processing, and check system stability, respectively. The stability check result was required to be less than 5%.

For the ISS measurements, to ensure the accuracy of the results, two punches were cut from each sample, and three sets of spectral data were recorded for each punch. The final sample spectrum was obtained by averaging the six sets of data. The dark spectrum within the integrating sphere over the wavelength range of 370–880 nm was recorded with the light source turned off and was removed as the instrumental background during calculation. To verify the accuracy of the method and improve its reliability, in addition to the removal of instrumental background and repeated measurements, our research team also conducted preliminary experiments and calculated the methodological uncertainty. To eliminate the influence of compositional differences among different

samples, several lightly polluted samples and several heavily polluted samples were selected during the preliminary experiment stage for repeated measurements. Analysis of several long-time-sequence measurements showed that the spectral variation of all samples became nearly zero after they had been placed inside the integrating sphere for 3–4 min. Therefore, the complete solvent-stripping time was determined to be 3–4 min. During the formal experiments, a timer was used to ensure that the spectra of each sample were recorded after 5 min of solvent stripping.

In this study, the experimental design minimized sampling differences between PAX and ISS. The PAX and high-flow filter samplers were deployed near the same observation site, on the rooftop platform of the Chinese Research Academy of Environmental Sciences, approximately 10 m above ground, with no significant anthropogenic emission sources within an 80 m radius. The filter sampling period was from 09:00 each day to 08:30 the next day, totaling 23.5 h. PAX data were also screened and averaged over the same time window to obtain a 23.5 h mean $B_{abs\_coated}(870)$ corresponding to the filter samples. Therefore, PAX and ISS represent the same daily-scale, regional mixed $PM_{2.5}$ population, rather than two independent, unrelated aerosol populations.

This daily alignment does not, however, resolve intraday variability. AAE_{coated} is obtained from the daily-integrated filter, while $B_{abs\_coated}(870)$ is measured continuously by PAX and then averaged over the same 23.5 h period. If the spectral slope and the 870 nm absorption magnitude covary within a day, combining one daily AAE_{coated} with the daily-averaged PAX value can smooth this covariance and may bias the reconstructed daily $B_{abs\_coated}(\lambda)$. The present framework therefore supports daily and longer-term comparisons but does not resolve diurnal changes in aerosol optical properties.

Regarding the differences between in situ observations and offline filter-based measurements, although ISS uses particles collected on filters, its measurement principle is not equivalent to conventional filter-based attenuation or absorption

methods and does not require the same type of empirical corrections for scattering losses, filter multiple scattering, and loading effects as traditional transmission- or reflection-based filter absorption methods (Wonaschütz et al., 2009). The reasons are as follows:

First, in ISS calculations, the relative light intensity between a loaded filter and a blank filter is used. The blank filter, having the same size, filter material, solvent, and cuvette conditions, serves as a reference. As a result, the background absorption of the filter itself, as well as the optical effects of the solvent and cuvette, are largely subtracted.

Second, the integrating sphere's inner wall has high diffuse reflectivity, which maximizes the collection of light scattered by the filter and particles. Compared with conventional transmission/reflection-based filter optical methods, ISS is less sensitive to misinterpreting scattering losses as absorption.

Third, the CF used in ISS converts the absorption signal obtained under multi-directional light paths inside the integrating sphere into a one-way absorption signal comparable to PAX, thereby reducing systematic bias caused by differences in instrument geometry and optical path.

These quality control measures cannot completely eliminate uncertainty, but they can effectively reduce systematic biases caused by instrument drift, filter matrix effects, and operational differences.

Section S6 Comparison on different operational definitions of E_{abs}

There is broad agreement on the standard definition of the enhancement factor, E_{abs}, which refers to the enhancement of BC absorption caused by the lensing effect of coatings:

$$E_{abs} = \frac{B_{abc,BC}+B_{abc,lensing}}{B_{abc,BC}} = 1 + \frac{B_{abc,lensing}}{B_{abc,BC}} \quad (S5)$$

where $B_{abs,lensing}$ represents the absorption equivalent due solely to the lensing effect, and $B_{abs,BC}$ represents the absorption coefficient of BC in the absence of lensing.

If BC is assumed to be the only light-absorbing carbonaceous component in atmospheric aerosols, the absorption enhancement factor for BC can be understood simply as the ratio of absorption with and without a coating layer:

$$E_{abs} = \frac{B_{abs\_coated}}{B_{abs\_uncoated}} \quad (S6)$$

where, in this expression, the numerator B_{abs_coated} is $B_{abc,BC} + B_{abc,lensing}$, and the denominator $B_{abs\_uncoated}$ is $B_{abc,BC}$. This ratio can be obtained through thermal denuding or solvent dissolution.

However, as BrC has received increasing attention in recent years, results obtained from Equation (S6) using either thermal denuding or solvent dissolution approaches are effectively equivalent to those from Equation (S7):

$$E_{abs} = \frac{B_{abs\_coated}}{B_{abs\_uncoated}} = \frac{B_{abs,BC}+B_{abs,BrC}+B_{abs,lensing}}{B_{abs,BC}} \quad (S7)$$

Compared with the standard definition of E_{abs} in Equation (S5), the numerator in Equation (S7) contains an additional contribution, namely $B_{abs,BrC}$. As a result, E_{abs} values calculated using Equation (S7) are theoretically higher than those calculated using Equation (S5). Numerous studies have calculated E_{abs} following the logic of Equation (S7), including studies using thermal denuding (Cappa et al., 2012; Fu et al., 2021; Xie et al., 2019) and solvent dissolution (Chen et al., 2017; Cui et al., 2016; Lan et al., 2024).

Another ISS-based approach directly divides the absorption coefficient measured by PAX ($B_{abs,BC}$+$B_{abs,BrC}$+$B_{abs,lensing}$) by that obtained from ISS ($B_{abs,BC}$+$B_{abs,BrC}$) to

derive E_{abs} (Li et al., 2023):

$$E_{abs}=\frac{B_{\text{abs\_coated}}}{B_{\text{abs\_uncoated}}}=\frac{B_{\text{abs,BC}}+B_{\text{abs,BrC}}+B_{\text{abs,lensing}}}{B_{\text{abs,BC}}+B_{\text{abs,BrC}}}=1+\frac{B_{\text{abs,lensing}}}{B_{\text{abs,BC}}+B_{\text{abs,BrC}}} \quad \text{(S8)}$$

In this definition, both the numerator and the denominator include BrC absorption. Compared with Equation (S5), Equation (S8) represents the enhancement relative to ($B_{\text{abs,BC}}$+$B_{\text{abs,BrC}}$) rather than solely relative to $B_{\text{abs,BC}}$. Consequently, values calculated using Equation (S8) are slightly lower than those calculated using Equation (S5).

Based on the above analysis, the expected high-to-low sequence of reported E_{abs} values is (S7) > (S5) > (S8) in theory.

Each equation above is valid within its own methodological framework and provides useful insight into BC absorption enhancement, provided that its meaning is clearly understood.

Section S7 Assessment of uncertainty of PAX-ISS methodology

The uncertainty analysis considers the propagation of uncertainties from the PAX-ISS measurements and related parameters. These uncertainties should be considered when interpreting wavelength-dependent variations in absorption enhancement and the possible influence of BrC blocking effects.

Using the PAX-ISS hybrid framework, this study decomposes total aerosol absorption into contributions from BC, BrC, and the lensing effect and ultimately determines the absorption enhancement factor (E_{abs}) from multiple measured and derived quantities. Therefore, the evaluation should follow error-propagation principles and should be based on a clear identification of the uncertainty sources and characteristics of each relevant sub-variable.

In the manuscript, E_{abs} is expressed as follows:

$$E_{\mathrm{abs}}(\lambda) = \frac{B_{\mathrm{abs,BC}}(\lambda) + B_{\mathrm{abs\_lensing}}(\lambda)}{B_{\mathrm{abs,BC}}(\lambda)}$$

$$= \frac{B_{\mathrm{abs,BC}}(\lambda)+(B_{\mathrm{abs\_coated}}(\lambda)-B_{\mathrm{abs\_uncoated}}(\lambda))}{B_{\mathrm{abs,BC}}(\lambda)}$$

$$= \frac{B_{\mathrm{abs,BC}}(\lambda)+(B_{\mathrm{abs\_coated}}(870)\times\left(\frac{\lambda}{870}\right)^{-AAE_{\mathrm{coated}}} - \frac{100\times ABS_{\mathrm{ISS}}\times A}{CF\times F\times T})}{B_{\mathrm{abs,BC}}(\lambda)} \quad \text{(S9)}$$

where $B_{\mathrm{abs,BC}}(\lambda)$ is the absorption coefficient of BC; $B_{\mathrm{abs,BrC}}(\lambda)$ is the absorption coefficient of BrC; $B_{\mathrm{abs,lensing}}(\lambda)$ is the absorption coefficient due to the lensing effect; $B_{\mathrm{abs,coated}}(\lambda)$ is the total absorption coefficient of coated aerosols; $B_{\mathrm{abs,uncoated}}(\lambda)$ is the lensing-free absorption coefficient; λ is the wavelength; AAE_{coated} is the absorption Ångström exponent of coated aerosols; CF is the correction factor; A is the deposited area on the filter; F is the sampling flow rate; T is the sampling duration, and ABS_{ISS} is the absorbance of the filter sample measured by ISS.

Thus, the uncertainty of $E_{\mathrm{abs}}(\lambda)$ results from the propagation of uncertainties in the five sub-variables $B_{\mathrm{abs,BC}}(\lambda)$, $B_{\mathrm{abs\_coated}}(870)$, AAE_{coated}, CF, and ABS_{ISS}. We discuss the probability distributions of these five sub-variables in turn..

(1) $B_{\mathrm{abs\_coated}}(870)$. The value of $B_{\mathrm{abs\_coated}}(870)$ is obtained primarily from

direct PAX measurements and may be influenced by instrument calibration, laser-intensity stability, flow-rate stability, cavity contamination, relative humidity, and acoustic response. According to Lack et al. (2006), the PAX technique has become an accepted reference for comparisons with filter-based and difference methods (Arnott et al., 1999, 2003, 2005a, b; Moosmüller et al., 1998; Schmid et al., 2006; Schnaiter et al., 2005; Sheridan et al., 2005). Reported accuracies are typically 5–10%, depending on the laboratory or field setting and the calibration method. The overall instrument accuracy with respect to aerosol absorption is estimated to be about 5%. Lack et al. (2009) later reconfirmed this estimate. Therefore, the uncertainty in $B_{\mathrm{abs\_coated}}$ was taken as 5%.

(2) AAE_{coated}. Because the PAX instrument used in this study is a single-wavelength PAX-870, only the in situ absorption at 870 nm ($B_{\mathrm{abs\_coated}}(870)$) was measured directly. We calculated AAE_{coated} from the power-law relationship between wavelength and the light-absorption signals obtained using the multi-wavelength thermal/optical carbon analyser (Chen et al., 2015; Chow et al., 2018, 2021; Shen et al., 2025). Based on $B_{\mathrm{abs\_coated}}(870)$ and AAE_{coated}, we then calculated the absorption coefficient at any wavelength between 370 and 880 nm, namely $B_{\mathrm{abs\_coated}}(\lambda)$.

We examined the absorption-coefficient fitting results for a representative day, as shown in the figure below and in Figure S3 of the Supplement. Based on the differences between the measured absorption coefficients at the seven wavelengths and the corresponding values derived from the fitted curve, we estimated the uncertainty of *AAE* to be 3.6%.

The 3.6% estimate reflects the scatter around the fitted seven-wavelength relationship for the representative sample and does not necessarily capture every systematic uncertainty in the filter-derived AAE_{coated}. Residual positive or negative filter artefacts and sampling-induced changes in particle morphology, if present, could propagate through extrapolated $B_{\mathrm{abs\_coated}}(\lambda)$ to $B_{\mathrm{abs,lensing}}(\lambda)$ and $E_{\mathrm{abs}}(\lambda)$, particularly at wavelengths farther from the directly measured 870 nm PAX channel. The short-

wavelength results should therefore be interpreted cautiously.

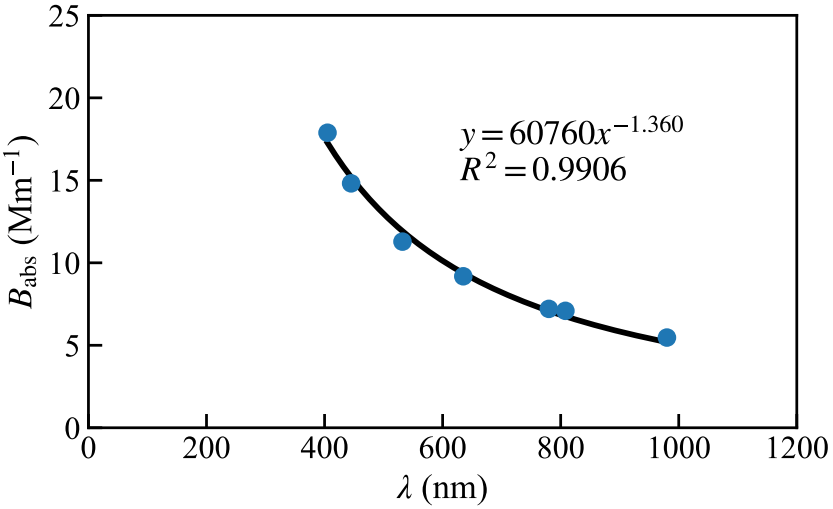

Figure S3 Absorption coefficients and the fitted curve measured by the DRI Model 2015 Multi-Wavelength Thermal/Optical Carbon Analyser on 19 February 2023.

(3) ABS_{ISS}. ABS_{ISS} is the fundamental quantity used to calculat $B_{abs\_uncoated}(\lambda)$ (defined as $B_{abs\_uncoated}(\lambda) = \frac{100 \times ABS_{ISS} \times A}{CF \times F \times T}$). The uncertainty in ABSISS measurements arises from factors including the stability of the integrating-sphere light source, detector response, repeatability of sample punches, uniformity of filter deposition, solvent treatment time, blank-filter subtraction, and variations in sample positioning within the integrating sphere. According to Wonaschütz et al. (2009), the precision of ISS-measured absorbance is 4%.

(4) CF. As described in our manuscript, the punch placed in the cuvette inside the integrating sphere chamber can absorb light from multiple directions rather than from a single direction. This causes the absorbance measured by the ISS system to differ from that measured by a conventional method, in which the incident light travels along one direction. The conversion factor (CF), which converts ISS-measured absorbance to conventional one-way absorbance, was determined by comparing the absorbance values of Humic Acid Sodium Salt (HASS) obtained using ISS (ABS_{ISS}) and a conventional setup (ABS_o; e.g., a cuvette outside the integrating sphere). We refer to our previous article (Li et al., 2023), where the determination of CF was described. The relative standard deviation (RSD) of the measured ABS_{ISS} was 5.67% (Li et al., 2023).

(5) $B_{abs,BC}(\lambda)$. The uncertainty in $B_{abs,BC}(\lambda)$ primarily stems from the decomposition of ABS_{ISS} value during the DWIC process, i.e., partitioning it into the contribution shares of BC and BrC. For evaluation, we used the data from Wonaschütz et al. (2009), who measured a series of reference samples containing known proportions of carbon black and humic acid sodium salt using the DWIC method and assessed the performance of DWIC in decomposing the absorbance contributions of BC and BrC. They plotted attenuation signals calculated from calibration curves against attenuation signals directly measured by ISS, as shown in Figure 3 of Wonaschütz et al. (2009), with one scatter plot for long-wavelength values and another for short-wavelength values. Using the open-source WebPlotDigitizer software, we extracted the x- and y-coordinates of each data point directly (see Table S3 in the Supplement). The results show that the average relative difference for $B_{abs,BC}(\lambda)$ was 10.4% at the low wavelength and 8.1% at the high wavelength.

After determining the uncertainties of all five sub-variables, we propagated them to estimate the uncertainty of E_{abs}. We used Monte Carlo simulation to calculate the probability distribution of E_{abs} for the sample collected on 19 February 2023. As shown below and in Figure S4, the mean E_{abs} at 420 nm is 1.789 ± 0.221, corresponding to an uncertainty of 12.4%; at 650 nm, the mean E_{abs} is 2.324 ± 0.189, corresponding to an uncertainty of 8.1%.

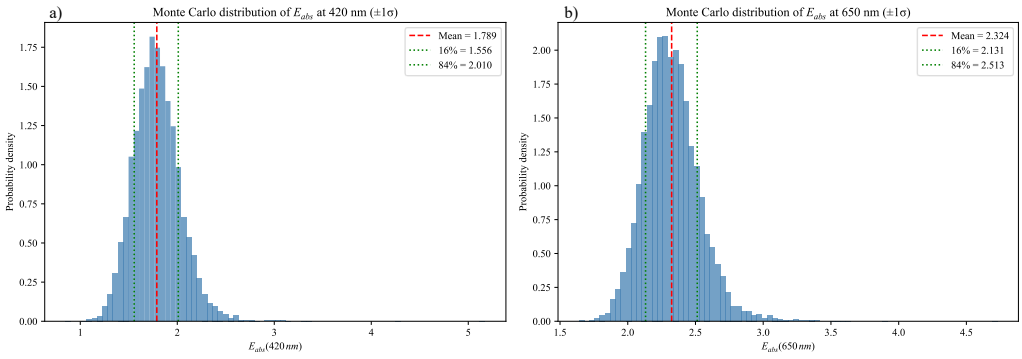

Figure S4 Probability distribution of E_{abs} at 420nm (a) and 650nm (b) on 19 February 2023. The ±1σ range (68% probability) is used to represent uncertainty.

For $B_{\mathrm{abs,lensing}}(\lambda)$ alone, the uncertainty results from the propagation of uncertainties in the four sub-variables ($B_{\mathrm{abs_{coated}}}(870)$, AAE_{coated}, CF, and ABS_{ISS}) used to calculate $B_{\mathrm{abs,lensing}}(\lambda)$. Because the uncertainties of these four sub-variables have been determined, we used Monte Carlo simulation to calculate the probability distribution of $B_{\mathrm{abs,lensing}}(\lambda)$ for the sample collected on 19 February 2023. As shown below and in Figure S5, the mean $B_{\mathrm{abs,\,lensing}}$ at 420 nm is 0.939 ± 0.246 $\mathrm{Mm^{-1}}$, corresponding to an uncertainty of 26.2%; at 650 nm, the mean $B_{\mathrm{abs,\,lensing}}$ is 0.958 ± 0.105 $\mathrm{Mm^{-1}}$, corresponding to an uncertainty of 11.0%.

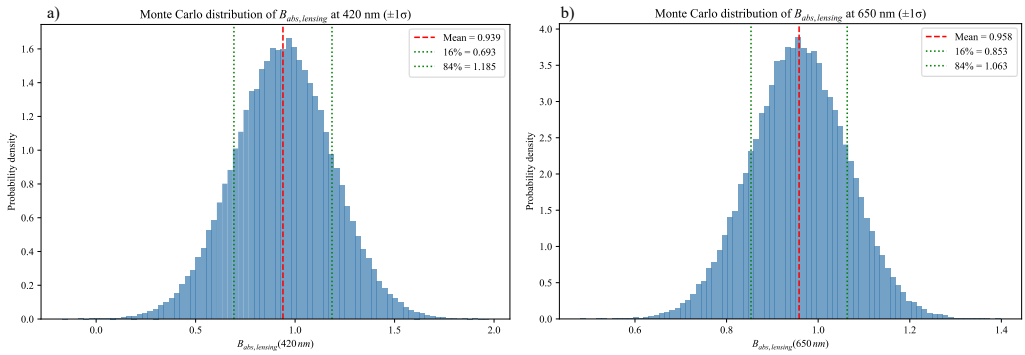

Figure S5 Probability distributions of $B_{\mathrm{abs,lensing}}$ at 420 nm (a) and 650 nm (b) on 19 February 2023. The ±1σ range (68% probability) is used to represent uncertainty.

386 **Table S3** Data extracted from Figure 3 of Wonaschütz et al. (2009) using the open-source

387 WebPlotDigitizer software

Wavelength (nm)	Types of light-absorbing carbon	Measured attenuation (x)	Calculated attenuation (y)	Residual (y-x)	Relative residual (%)
404	BC	0.0378	0.0395	0.0017	4.497354
404	BC	0.0472	0.0421	-0.0051	10.80508
404	BC	0.0489	0.052	0.0031	6.339468
404	BC	0.0615	0.0575	-0.004	6.504065
404	BC	0.0646	0.0679	0.0033	5.108359
404	BC	0.0713	0.0769	0.0056	7.854137
404	BC	0.0786	0.0753	-0.0033	4.198473
404	BC	0.0808	0.0894	0.0086	10.64356
404	BC	0.0875	0.0854	-0.0021	2.4
404	BC	0.0899	0.1019	0.012	13.34816
404	BC	0.0955	0.1119	0.0164	17.17277
404	BC	0.0979	0.1007	0.0028	2.860061
404	BC	0.0984	0.1211	0.0227	23.06911
404	BC	0.1079	0.1337	0.0258	23.91103
404	BC	0.1101	0.1144	0.0043	3.90554
404	BC	0.1124	0.1253	0.0129	11.47687
404	BC	0.119	0.1361	0.0171	14.36975
404	BC	0.1274	0.1503	0.0229	17.97488
404	BrC	0.0209	0.0228	0.0019	9.090909
404	BrC	0.0353	0.0333	-0.002	5.665722
404	BrC	0.0481	0.0451	-0.003	6.237006
404	BrC	0.0631	0.0593	-0.0038	6.022187
404	BrC	0.0805	0.0783	-0.0022	2.732919
404	BrC	0.0873	0.0895	0.0022	2.520046
404	BrC	0.0991	0.1044	0.0053	5.348133
404	BrC	0.1083	0.1194	0.0111	10.24931
404	BrC	0.1145	0.1311	0.0166	14.49782
404	BrC	0.1193	0.1419	0.0226	18.94384
404	BrC	0.1278	0.1571	0.0293	22.92645
650	BC	0.0156	0.0143	-0.0013	8.333333
650	BC	0.028	0.0232	-0.0048	17.14286
650	BC	0.0386	0.032	-0.0066	17.09845
650	BC	0.0498	0.0424	-0.0074	14.85944
650	BC	0.0526	0.0452	-0.0074	14.06844
650	BC	0.0653	0.0566	-0.0087	13.32312
650	BC	0.0676	0.0605	-0.0071	10.50296
650	BC	0.0748	0.0674	-0.0074	9.893048
650	BC	0.0834	0.0765	-0.0069	8.273381
650	BC	0.0854	0.0817	-0.0037	4.332553
650	BC	0.093	0.0878	-0.0052	5.591398
650	BC	0.0952	0.0939	-0.0013	1.365546
650	BC	0.0983	0.096	-0.0023	2.339776
650	BC	0.1011	0.1034	0.0023	2.274975
650	BC	0.1054	0.1049	-0.0005	0.474383

650	BC	0.1066	0.1122	0.0056	5.253283
650	BC	0.1133	0.1163	0.003	2.647838
650	BC	0.1153	0.1244	0.0091	7.892454
650	BrC	0.0113	0.0133	0.002	17.69912
650	BrC	0.0207	0.0209	0.0002	0.966184
650	BrC	0.0307	0.0284	-0.0023	7.491857
650	BrC	0.0396	0.0392	-0.0004	1.010101
650	BrC	0.0532	0.0522	-0.001	1.879699
650	BrC	0.0599	0.0601	0.0002	0.33389
650	BrC	0.0682	0.0708	0.0026	3.812317
650	BrC	0.0765	0.081	0.0045	5.882353
650	BrC	0.0823	0.0889	0.0066	8.019441
650	BrC	0.0858	0.0966	0.0108	12.58741
650	BrC	0.095	0.1071	0.0121	12.73684

Reference

Arnott, W. P., Hamasha, K., Moosmüller, H., Sheridan, P. J., and Ogren, J. A.: Towards aerosol light-absorption measurements with a 7-wavelength aethalometer: Evaluation with a photoacoustic instrument and 3-wavelength nephelometer, Aerosol Sci. Technol., 39, 17–29, https://doi.org/10.1080/027868290901972, 2005b.

Arnott, W. P., Moosmüller, H., Rogers, C. F., Jin, T., and Bruch, R.: Photoacoustic spectrometer for measuring light absorption by aerosol: Instrument description, Atmos. Environ., 33, 2845–2852, https://doi.org/10.1016/S1352-2310(98)00361-6, 1999.

Arnott, W. P., Moosmüller, H., Sheridan, P. J., Ogren, J. A., Raspet, R., Slaton, W. V., Hand, J. L., Kreidenweis, S. M., and Collett, J. L.: Photoacoustic and filter-based ambient aerosol light absorption measurements: Instrument comparisons and the role of relative humidity, J. Geophys. Res., 108, 4034, https://doi.org/10.1029/2002JD002165, 2003.

Arnott, W. P., Zielinska, B., Rogers, C. F., Sagebiel, J., Park, K., Chow, J., Moosmüller, H., Watson, J. G., Kelly, K., Wagner, D., Sarofim, A., Lighty, J., and Palmer, G.: Evaluation of 1047-nm photoacoustic instruments and photoelectric aerosol sensors in source-sampling of black carbon aerosol and particle-bound PAHs from gasoline and diesel powered vehicles, Environ. Sci. Technol., 39, 5398–5406, https://doi.org/10.1021/es049595e, 2005a.

Cappa, C. D., Onasch, T. B., Massoli, P., Worsnop, D. R., Bates, T. S., Cross, E. S., Davidovits, P., Hakala, J., Hayden, K. L., Jobson, B. T., Kolesar, K. R., Lack, D. A., Lerner, B. M., Li, S.-M., Mellon, D., Nuaaman, I., Olfert, J. S., Petäjä, T., Quinn, P. K., Song, C., Subramanian, R., Williams, E. J., and Zaveri, R. A.: Radiative absorption enhancements due to the mixing state of atmospheric black carbon, Science, 337, 1078–1081, https://doi.org/10.1126/science.1223447, 2012.

Chen, B., Bai, Z., Cui, X., Chen, J., Andersson, A., and Gustafsson, Ö.: Light absorption enhancement of black carbon from urban haze in northern China winter, Environ. Pollut., 221, 418–426, https://doi.org/10.1016/j.envpol.2016.12.004, 2017.

Chen, L. W. A., Chow, J. C., Wang, X. L., Robles, J. A., Sumlin, B. J., Lowenthal, D. H.,

Zimmermann, R., and Watson, J. G.: Multi-wavelength optical measurement to enhance thermal/optical analysis for carbonaceous aerosol, Atmos. Meas. Tech., 8, 451–461, https://doi.org/10.5194/amt-8-451-2015, 2015.

Cheng, Y., Zheng, M., He, K., Chen, Y., Yan, B., Russell, A. G., Shi, W., Jiao, Z., Sheng, G., Fu, J., and Edgerton, E. S.: Comparison of two thermal-optical methods for the determination of organic carbon and elemental carbon: Results from the southeastern United States, Atmos. Environ., 45, 1913–1918, https://doi.org/10.1016/j.atmosenv.2011.01.036, 2011.

Chow, J. C., Chen, L.-W. A., Wang, X., Green, M. C., and Watson, J. G.: Improved estimation of PM2.5 brown carbon contributions to filter light attenuation, Particuology, 56, 1–9, https://doi.org/10.1016/j.partic.2021.01.001, 2021.

Chow, J. C., Watson, J. G., Green, M. C., Wang, X., Chen, L.-W. A., Trimble, D. L., Cropper, P. M., Kohl, S. D., and Gronstal, S. B.: Separation of brown carbon from black carbon for IMPROVE and Chemical Speciation Network PM2.5 samples, J. Air Waste Manage., 68, 494–510, https://doi.org/10.1080/10962247.2018.1426653, 2018.

Chung, C. E., Ramanathan, V., Kim, D., and Podgorny, I. A.: Global anthropogenic aerosol direct forcing derived from satellite and ground-based observations, J. Geophys. Res., 110, D24207, https://doi.org/10.1029/2005JD006356, 2005.

Cui, X., Wang, X., Yang, L., Chen, B., Chen, J., Andersson, A., and Gustafsson, Ö.: Radiative absorption enhancement from coatings on black carbon aerosols, Sci. Total Environ., 551–552, 51–56, https://doi.org/10.1016/j.scitotenv.2016.02.026, 2016.

Fu, Y., Peng, X., Guo, Z., Peng, L., Lin, Q., Li, L., Li, M., Chen, D., Zhang, G., Bi, X., Wang, X., and Sheng, G.: Filter-based absorption enhancement measurement for internally mixed black carbon particles over southern China, Sci. Total Environ., 762, 144194, https://doi.org/10.1016/j.scitotenv.2020.144194, 2021.

Kwon, D., Sovers, M. J., Grassian, V. H., Kleiber, P. D., and Young, M. A.: Optical Properties of Humic Material Standards: Solution Phase and Aerosol Measurements, ACS Earth Space Chem., 2, 1102–1111, https://doi.org/10.1021/acsearthspacechem.8b00097, 2018.

Lack, D. A., Cappa, C. D., Cross, E. S., Massoli, P., Ahern, A. T., Davidovits, P., and Onasch, T. B.:

Absorption enhancement of coated absorbing aerosols: Validation of the photo-acoustic technique for measuring the enhancement, Aerosol Sci. Technol., 43, 1006–1012, https://doi.org/10.1080/02786820903117932, 2009.

Lack, D. A., Lovejoy, E. R., Baynard, T., Pettersson, A., and Ravishankara, A. R.: Aerosol absorption measurement using photoacoustic spectroscopy: Sensitivity, calibration, and uncertainty developments, Aerosol Sci. Technol., 40, 697–708, https://doi.org/10.1080/02786820600803917, 2006.

Lan, Y., Zhou, L., Liu, S., Wan, R., Wang, N., Chen, D., Li, Y., Jiang, Y., Rao, Z., Jiang, W., Song, D., Tan, Q., and Yang, F.: Light absorption enhancement of black carbon and its impact factors during winter in a megacity of the Sichuan Basin, China, Sci. Total Environ., 918, 170374, https://doi.org/10.1016/j.scitotenv.2024.170374, 2024.

Li, H., McMeeking, G. R., and May, A. A.: Development of a new correction algorithm applicable to any filter-based absorption photometer, Atmos. Meas. Tech., 13, 2865–2886, https://doi.org/10.5194/amt-13-2865-2020, 2020.

Li, Z., Zhi, G., Zhang, Y., Jin, W., Sun, J., Kong, Y., Shen, Y., and Zhang, H.: The integrating sphere system plus in-situ absorption monitoring: A new scheme to study absorption enhancement of black carbon in ambient aerosols, Sci. Total Environ., 892, 164355, https://doi.org/10.1016/j.scitotenv.2023.164355, 2023.

Lin, P., Aiona, P. K., Li, Y., Shiraiwa, M., Laskin, J., Nizkorodov, S. A., and Laskin, A.: Molecular Characterization of Brown Carbon in Biomass Burning Aerosol Particles, Environ. Sci. Technol., 50, 11815–11824, https://doi.org/10.1021/acs.est.6b03024, 2016.

Moosmüller, H., Arnott, W. P., Rogers, C. F., Chow, J. C., Frazier, C. A., Sherman, L. E., and Dietrich, D. L.: Photoacoustic and filter measurements related to aerosol light absorption during the Northern Front Range Air Quality Study (Colorado 1996/1997), J. Geophys. Res., 103, 28149–28157, https://doi.org/10.1029/98JD02618, 1998.

Peng, C., Yang, F., Tian, M., Shi, G., Li, L., Huang, R.-J., Yao, X., Luo, B., Zhai, C., and Chen, Y.: Brown carbon aerosol in two megacities in the Sichuan Basin of southwestern China: Light absorption properties and implications, Sci. Total Environ., 719, 137483,

https://doi.org/10.1016/j.scitotenv.2020.137483, 2020.

Radney, J. G. and Zangmeister, C. D.: Light source effects on aerosol photoacoustic spectroscopy measurements, J. Quant. Spectrosc. Radiat. Transf., 187, 145–149, https://doi.org/10.1016/j.jqsrt.2016.09.026, 2017.

Ram, K. and Sarin, M. M.: Absorption coefficient and site-specific mass absorption efficiency of elemental carbon in aerosols over urban, rural, and high-altitude sites in India, Environ. Sci. Technol., 43, 8233–8239, https://doi.org/10.1021/es9011542, 2009.

Schmid, O., Artaxo, P., Arnott, W. P., Chand, D., Gatti, L. V., Frank, G. P., Hoffer, A., Schnaiter, M., and Andreae, M. O.: Spectral light absorption by ambient aerosols influenced by biomass burning in the Amazon Basin. I: Comparison and field calibration of absorption measurement techniques, Atmos. Chem. Phys., 6, 3443–3462, https://doi.org/10.5194/acp-6-3443-2006, 2006.

Schnaiter, M., Schmid, O., Petzold, A., Fritzsche, L., Klein, K. F., Andreae, M. O., Helas, G., Thielmann, A., Gimmler, M., Möhler, O., Linke, C., and Schurath, U.: Measurement of wavelength-resolved light absorption by aerosols utilizing a UV-VIS extinction cell, Aerosol Sci. Technol., 39, 249–260, https://doi.org/10.1080/027868290925958, 2005.

Shen, Y., Zhi, G., Zhang, Y., Jin, W., Kong, Y., Li, Z., and Zhang, H.: An investigative review of the expanded capabilities of thermal/optical techniques for measuring carbonaceous aerosols and beyond, Environ. Pollut., 364, 125363, https://doi.org/10.1016/j.envpol.2024.125363, 2025.

Sheridan, P. J., Arnott, W. P., Ogren, J. A., Andrews, E., Atkinson, D. B., Covert, D. S., Moosmüller, H., Petzold, A., Schmid, B., Strawa, A. W., Varma, R., and Virkkula, A.: The Reno Aerosol Optics Study: An evaluation of aerosol absorption measurement methods, Aerosol Sci. Technol., 39, 1–16, https://doi.org/10.1080/027868290901891, 2005.

Sun, J., Zhang, Y., Zhi, G., Hitzenberger, R., Jin, W., Chen, Y., Wang, L., Tian, C., Li, Z., Chen, R., Xiao, W., Cheng, Y., Yang, W., Yao, L., Cao, Y., Huang, D., Qiu, Y., Xu, J., Xia, X., Yang, X., Zhang, X., Zong, Z., Song, Y., and Wu, C.: Brown carbon's emission factors and optical characteristics in household biomass burning: developing a novel algorithm for estimating the contribution of brown carbon, Atmos. Chem. Phys., 21, 2329–2341,

https://doi.org/10.5194/acp-21-2329-2021, 2021.

Virkkula, A., Mäkelä, T., Hillamo, R., Yli-Tuomi, T., Hirsikko, A., Hämeri, K., and Koponen, I. K.: A simple procedure for correcting loading effects of aethalometer data, J. Air Waste Manage., 57, 1214–1222, https://doi.org/10.3155/1047-3289.57.10.1214, 2007.

Wang, L., Jin, W., Sun, J., Zhi, G., Li, Z., Zhang, Y., Guo, S., He, J., and Zhao, C.: Seasonal features of brown carbon in northern China: Implications for BrC emission control, Atmos. Res., 257, 105610, https://doi.org/10.1016/j.atmosres.2021.105610, 2021.

Weingartner, E., Saathoff, H., Schnaiter, M., Streit, N., Bitnar, B., and Baltensperger, U.: Absorption of light by soot particles: determination of the absorption coefficient by means of aethalometers, J. Aerosol Sci., 34, 1445–1463, https://doi.org/10.1016/S0021-8502(03)00359-8, 2003.

Wonaschütz, A., Hitzenberger, R., Bauer, H., Pouresmaeil, P., Klatzer, B., Caseiro, A., and Puxbaum, H.: Application of the integrating sphere method to separate the contributions of brown and black carbon in atmospheric aerosols, Environ. Sci. Technol., 43, 1141–1146, https://doi.org/10.1021/es8008503, 2009.

Xie, C., Xu, W., Wang, J., Liu, D., Ge, X., Zhang, Q., Wang, Q., Du, W., Zhao, J., Zhou, W., Li, J., Fu, P., Wang, Z., Worsnop, D., and Sun, Y.: Light absorption enhancement of black carbon in urban Beijing in summer, Atmos. Environ., 213, 499–504, https://doi.org/10.1016/j.atmosenv.2019.06.041, 2019.